Tutorial on the basics of downward extrapolation operators

John C. Bancroft and Saleh M. Al-Saleh

ABSTRACT

There are many algorithms for downward extrapolating a seismic time section for migration. This tutorial demonstrates the downward extrapolation process, and focuses on the phase-shift extrapolator. A phase-shift extrapolator that is defined in (k_x, ω) space can be applied in (x, ω) space as a convolution operator to enable a spatially varying velocity. Truncating the spatial operator to an economical size in (x, ω) causes operator instability. This instability occurs when the truncated operator is applied recursively, and any amplitudes in (k_x, ω) space that exceed unity will tend to a very large number.

These concepts are illustrated with numerous diagrams, and a simple descriptive operator is presented to illustrate the effect of operator size and the amplitude of the sinc ringing.

INTRODUCTION

Migration basics

We categorize migration algorithms into three main types:

1. Kirchhoff;
2. FK, and
3. Downward continuation.

Kirchhoff migration weights and sums energy in (x, t) space along a diffraction-shaped curve. This method is capable of all types of migration such as post- or prestack, time or depth, and is the workhorse of the seismic industry. The theory is based on the high-frequency, asymptotic integral solution to the wave equation.

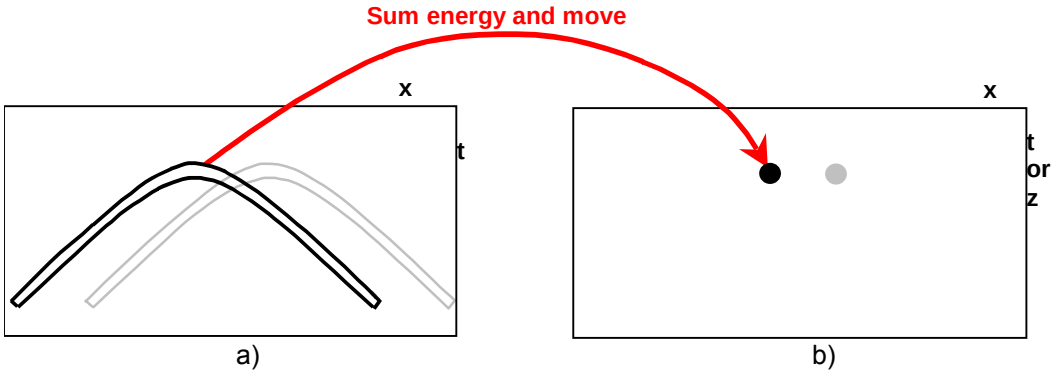

FIG. 1. Kirchhoff migration showing a summation window on the time section, and b) the summed energy located on the migrated section.

FK migration (frequency F – wavenumber K) produces ideal result in a constant-velocity medium. It is extremely fast and based on the Fourier transform of the wave

equation. It is useful for evaluating other migration algorithms, and has practical application in areas where the velocity is smoothly varying.

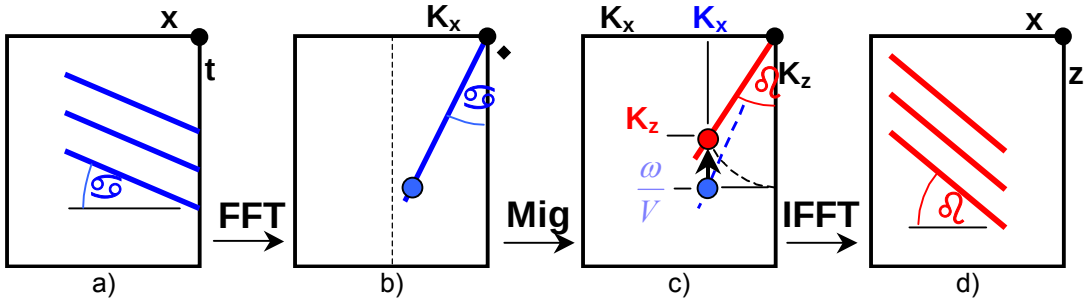

FIG. 2. FK migration illustration progressing from a) the input time section, b) the FK section, c) the migrated KK section, and d) the migrated depth section.

Downward continuation is a process that extrapolates the wavefield to simulate recordings at different depths below the surface. Energy in the time section is focused to reflectors at each depth level, and then mapped to a migrated section to form an image of the subsurface. The downward propagation of energy is based on various strategies for solving the wave equation such as finite-difference or Fourier transform methods. This method can account for the amplitude and phase of the propagating wavefield in media with variable properties and is the focus of this paper.

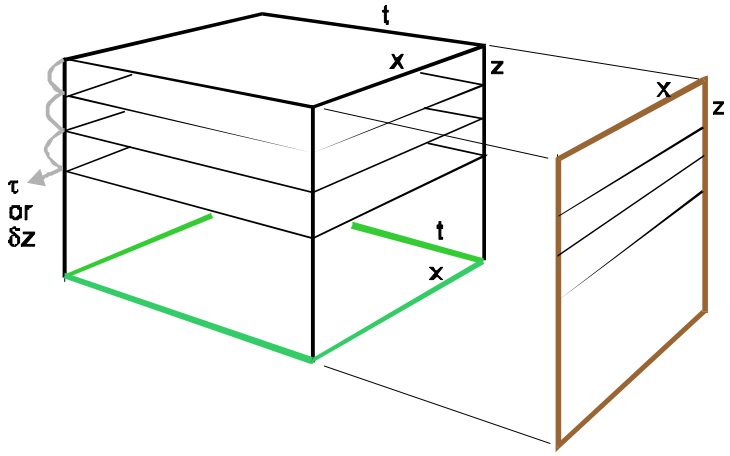

FIG. 3. Downward continuation migration with a depth migrated section on the right of the volume, and a migrated time section on the bottom of the volume.

Downward continuation of zero-offset data or post-stack migration

Energy from a source travels to a reflector, and then returns to the recording instrument. When the source and receiver are co-located, we assume that the energy travels along the same raypath to and from the reflector, and that the raypaths are normal to the reflector. We consider only one of these raypaths, and that is from the reflector to the surface. The recorded energy is then considered to have come from all reflectors and travelled along the corresponding raypaths to the surface through media with half the original velocity (because we are only using one-way time). This assumption is referred to as the Exploding Reflector Model, as energy is assumed to have left each reflector at the same time.

Downward continuation moves the reflected energy, in small depth increments, down the raypath, back to the reflector. The energy resides on the time section, but moves toward zero time with each depth increment. At a given depth, defined by the sum of the depth increments, the time section will appear as if it was recorded at that depth, and energy at zero time corresponds to reflectors at that depth. Therefore, at each downward increment, it is assumed that any energy at zero-time is energy focussed at that depth. This energy is then mapped to the corresponding depth on the migrated depth section.

The process is illustrated in Figure 4 that shows volume (*x, z, t*) with time sections that are repeated at different depth increments δz. At each depth level, the energy at zero time is copied to the corresponding depth on the migrated depth section, as indicated by the red highlights.

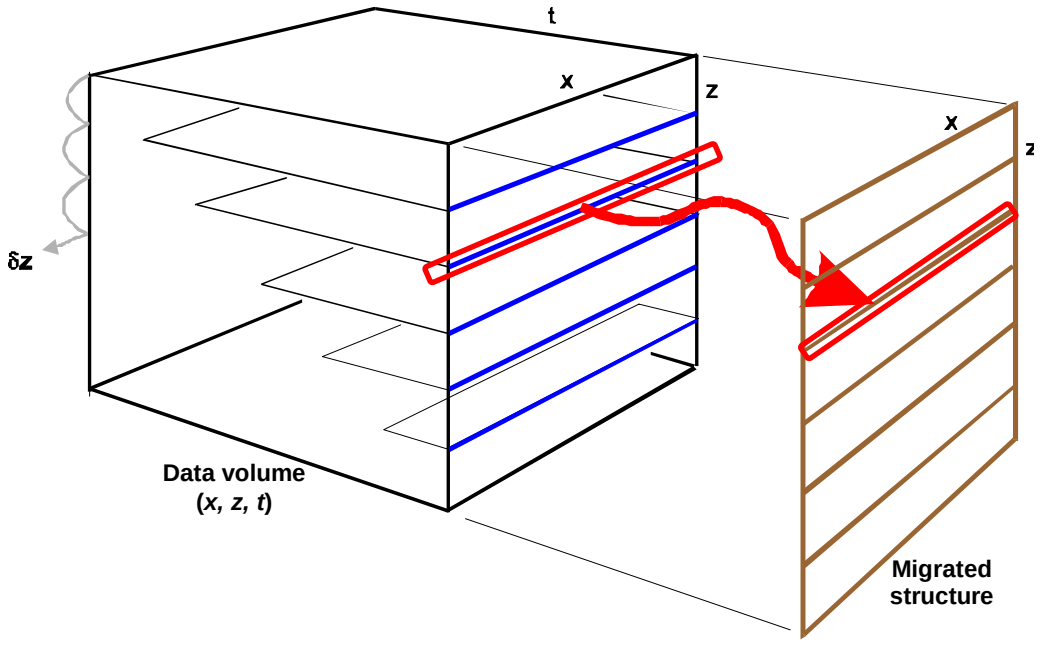

FIG. 4. Downward continuation depth migration showing the time section at varying depth intervals, and the migrated depth section.

Prestack downward continuation

Prestack data in source (shot) gathers may also be downward continued. We will now assume point reflectors and that energy is scattered back to the surface from these points that we call scatterpoints. The shape of the scattered energy is independent of the source location, and only dependent on the depth of the scatterpoint and the propagation velocities to the surface as illustrated in Figure 5. This figure shows scatterpoints at a fixed depth in a constant velocity medium, and the corresponding diffractions on a source gather, each with the same shape.

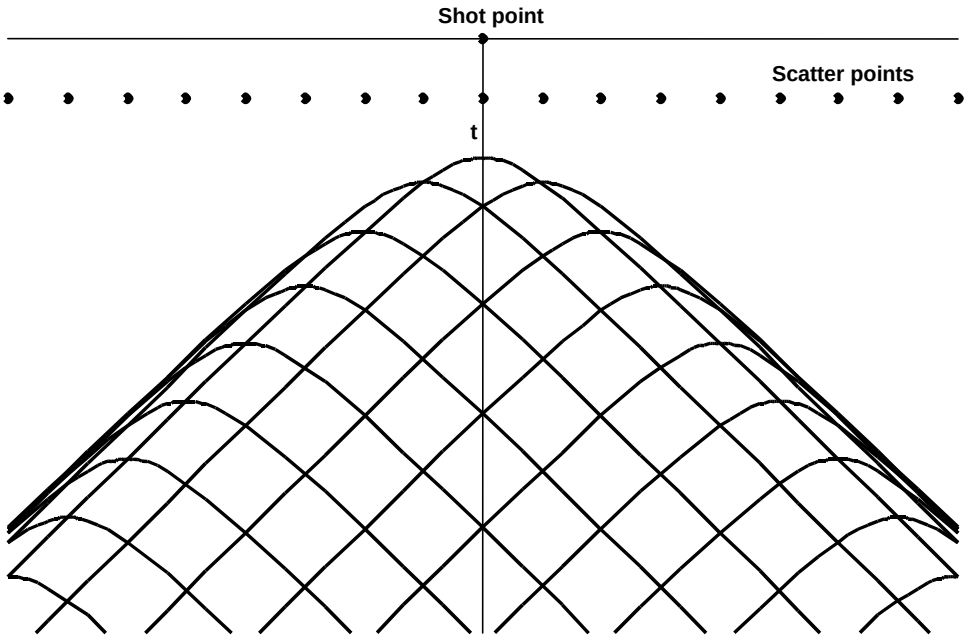

FIG. 5 A source-record that displays the energy from scatterpoints at a fixed depth.

With these assumptions, downward continuation of a source gather effectively lowers only the receivers into the subsurface as illustrated in Figure 6, which shows the focusing of the diffraction energy at two depths corresponding to the depths of the two shallowest rows of scatterpoints.

We now have a number of ways to continue processing, such as:

1. Using Kirchhoff methods to estimate the traveltime location of the scatterpoint and map the energy to the migrated source record.

2. Sort the data into receiver gathers and then, using the principle of reciprocity, downward continue the sources. This method of alternately downward-continuing both source and receiver gathers will focus the reflection energy to zero time and zero offset.

3. Model the wavefield from the source location, then use the incident and reflected wavefields to estimate the impedance of a reflector at the location of the scatterpoint.

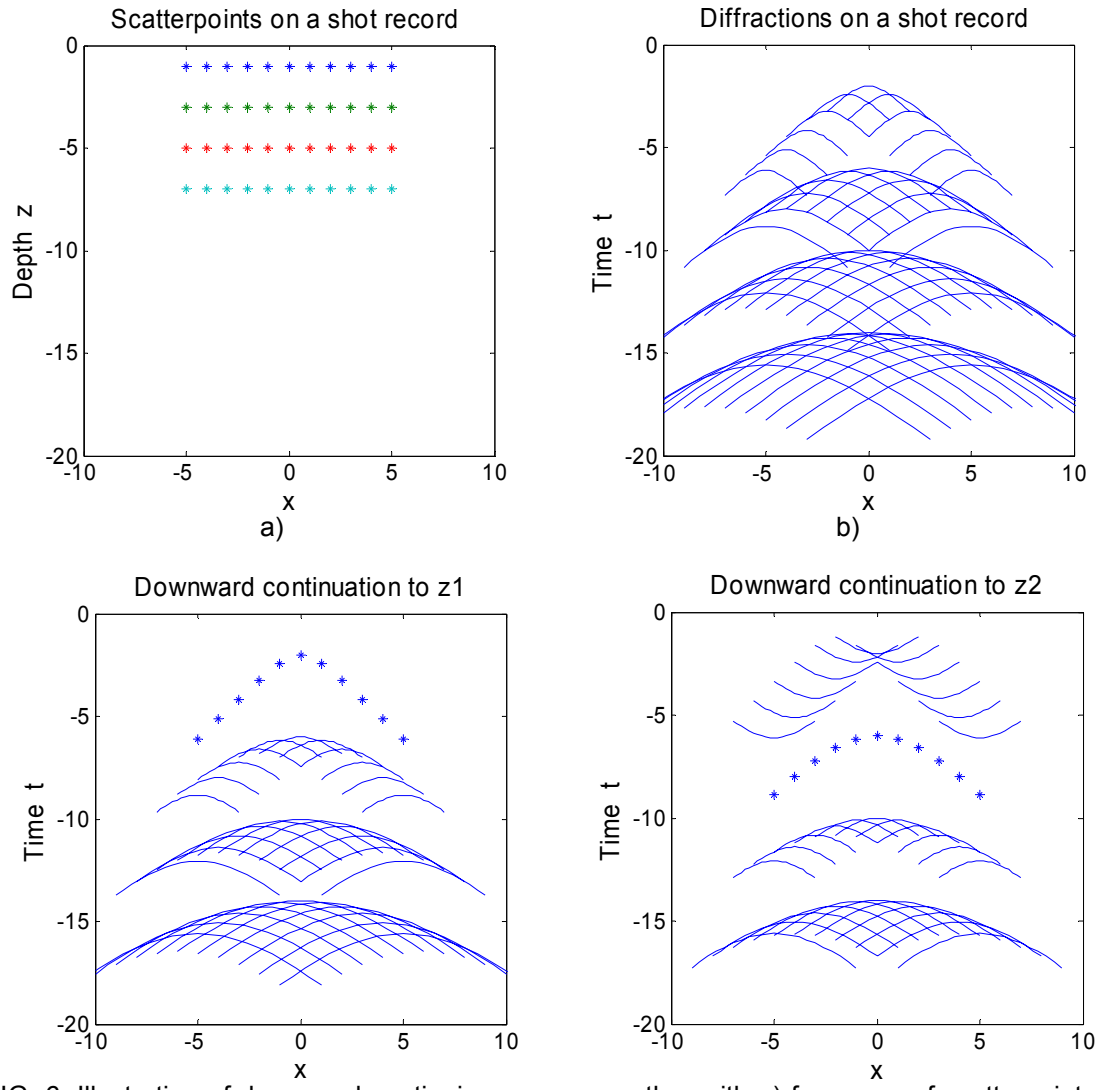

FIG. 6. Illustration of downward continuing a source gather with a) four rows of scatterpoints, b) the diffractions on a source record, c) downward continuing the source record to a depth of the first scatterpoint layer, and d) to the second layer. (`2004\ShotDif.m`)

Unfortunately, the distribution of energy from a scatterpoint on a constant offset section cannot be directly modelled or migrated with wave propagation techniques and cannot be migrated with conventional downward extrapolation algorithms.

DOWNWARD CONTINUATION ALGORITHMS

Finite-difference downward continuation

Wavefield propagation from one depth to another may be accomplished by finite-difference techniques. These methods use the Fourier transform of the wave equation to define a one-way form that essentially defines a first-order derivative in the depth direction. Finite differences of the first and second order derivatives are then used to propagate the wavefield.

Figure 7 illustrates 2-D 15- and 45-degree finite-difference solutions. The known sample values on the grid are identified by small spheres, while the larger spheres are the

samples being computed. The upper grid is the known time section at a depth level n, while the lower grid n+1 is being computed. Computations start at the maximum time level and compute all samples along i at that maximum time at j_{max}. The next time level at j_{max} - 1 is then computed, and the process repeated until the new time section is completed.

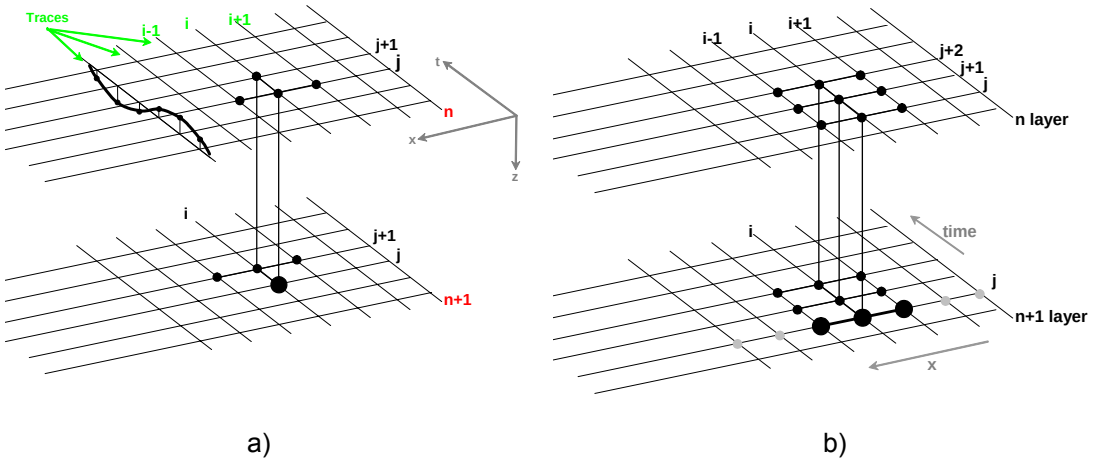

FIG. 7. Finite-difference operators in a grid, with a) an explicit 15-degree solution, and b) an implicit 45-degree solution.

The finite-difference solutions have a stability requirement that limits the size of the downward depth increment. However the size of the operator in (x, t) space is very small and the constant velocity assumption only applies to the size of the operators. Consequently the finite-difference approach is well suited for structures with heterogeneous velocities that vary in (x, y, z) space. In contrast, the following phase-shift method can only be applied to transverse homogeneous layers $V(z)$. Other methods that are based on the phase-shift solution will require some approximation to the constant velocity assumption.

Phase-shift downward continuation

The phase-shift method also Fourier transforms a constant density wave equation,

$$\frac{\partial^2 P}{\partial x^2} + \frac{\partial^2 P}{\partial z^2} = \frac{1}{v^2}\frac{\partial^2 P}{\partial t^2}, \qquad (1)$$

to give,

$$k_x^2 + k_z^2 = \frac{\omega^2}{v^2}, \qquad (2)$$

where v is the velocity. This form of the wave equation allows us to separate the upward and downward propagating wavefields (with some assumptions) by defining k_z as a square-root:

$$k_z = \pm \sqrt{\frac{\omega^2}{v^2} - k_x^2} \quad . \tag{3}$$

We can approximate the square root with a series expansion,

$$k_z \approx \pm \frac{\omega}{v}\left(1 - \frac{v^2 k_x^2}{2\omega^2} + \ldots\right), \tag{4}$$

that leads to a finite-difference solution (15-degree), but we will go directly to the phase-shift solution that uses the complete square root. We do this by taking the inverse Fourier transform in the z direction of the square-root Equation (3) to get a very simple first-order differential equation:

$$\frac{d\,P(z)}{d\,z} = -j\sqrt{\frac{\omega^2}{v^2} - k_x^2}\; P(z) = aP(z). \tag{5}$$

Note the variables k_x and ω are independent of z, and we assume that v is constant at this depth level. The solution is the exponential function

$$P(z) = e^{az}. \tag{6}$$

Adding a Δz term to z to get the downward continuation step increment, we get

$$P(z+\Delta z) = e^{a(z+\Delta z)} = e^{az}e^{a\Delta z} = P(z)e^{a\Delta z}. \tag{7}$$

Expressing the equation with all variables we get out final form of the equation,

$$P(k_x, z+\Delta z, \omega) = P(k_x, z, \omega)\, e^{-j\Delta z\sqrt{\frac{\omega^2}{v^2} - k_x^2}}. \tag{8}$$

This equation tells us that we can downward propagate seismic data in (k_x, ω) space by a simple complex multiplication as illustrated in Figure 8.

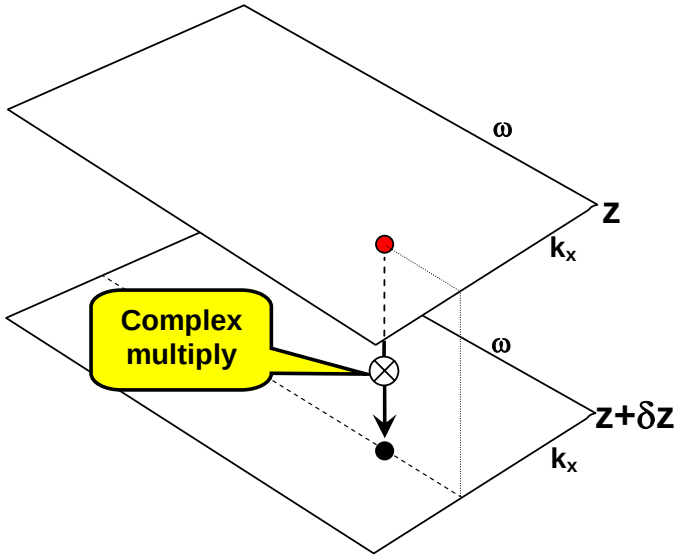

FIG. 8. Phase-shift migration is illustrated with a complex multiply of each sample in (k_x, ω) space.

The data however, must be in transformed space (k_x, ω) where we have lost any special dependence in x: i.e., the velocity v must be constant for this downward continuation step. However, the velocity may vary for each downward step, enabling the phase-shift migration to produce ideal results in a medium where the velocities vary with depth, i.e. $v(z)$. The output of the time section at zero time (x, $t=0$) required use of the inverse Fourier transform.

The *ωX* method

A number of algorithms were developed to allow lateral velocity variations at each depth increment. One method, phase-shift plus interpolation (PSPI), repeated the downward step a number of times at the same depth level in (*kx, ω*) space, each with a different velocity, and then interpolated the result in either (*x, ω*) or (*x, t*) space. However, the method we are discussing in this section will compute the downward step in (*x, ω*) space.

The algorithm is based on the phase-shift method, but uses the spatial inverse Fourier transform of the phase-shift operator and is referred to as the "omegaX" or ***ωX*** method. (Note that some finite-difference methods that approximate the derivatives in the Fourier transformed domain are also referred to as ***ωX*** methods are quite different than this method.) With the data in (*x, ω*) space, an entire spatial line, at a given frequency, can be processed to produce any single point in the extrapolated layer as illustrated in Figure 5. At this point, it is assumed that the velocity is constant over the spatial input data that is identified by the larger pink ellipse. However, we will assume the velocity is only constant over a smaller spatial extent of the initial layer as illustrated by the smaller red ellipse. Moving the centre of the small ellipse in Figure 9, to a new spatial location allows a different spatial velocity to be used.

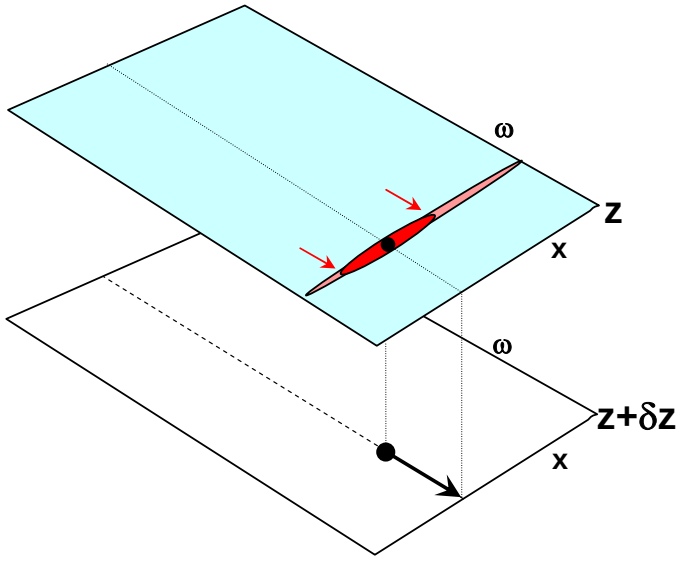

FIG. 9. Illustration of *ωX* migration where a line of data, at a given frequency, can be processed to one point in the downward-continued layer.

We now have an operator that can vary vertically and approximately in depth: i.e., *V(x, z)*. A large table of operators can be created for each velocity, at every frequency. The resulting convolutional process is time-consuming, so the operator is made as small as possible. Operators that are too short may have a stability problem, limited dips, or bandwidth reductions. The Inverse transform can also be applied again in the frequency direction to produce a phase-shift operation in the (*x, t*) space.

Phase-shift in (*x, t*) space

Inverse-transforming the ωX operator into (*x, t*) space defines an operator that maps a 2-D range of data at depth level *z* to one point on the new depth level $z+1$. This method is not really used as a downward extrapolator due to the computational overhead, but does provide a visual image of the shape and lateral extent of the operator in both (*x, t*) and (*x,* ω) space.

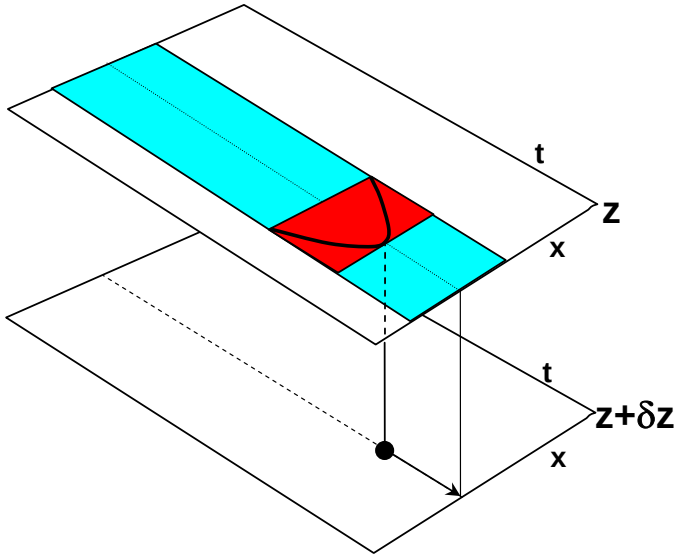

FIG. 10. Illustration of *Xt* downward extrapolation in (*x, t*) space.

The phase-shift operator in (*x, t*) space enables the visualization of an "ideal" or direct Kirchhoff diffraction operator mentioned above. Since the phase-shift operator can map energy from the surface at $z = 0$ to any depth, it enables the definition of a Kirchhoff operator that sums energy on an input time-section directly to a sample on the migrated section. The ideal diffraction shape, amplitude distribution, and phase-shift are contained in this 2-D operator.

The (*x, t*) phase-shift operator does assume a constant velocity; however, in time migrations, that constant velocity assumption is replaced by an RMS-type velocity, which does assume the velocity to be constant at a given (*x*, *z*, or *t*) location. Visualization of this operator enables a comparison between the line integral (summation) of a typical Kirchhoff migration with an "ideal" 2-D operator.

A PHASE-SHIFT MIGRATION EXAMPLE

Model data (`MOD50.SGY`) shown in Figure 11a was migrated using the phase-shift method. This model has 256 traces at 100-ft spacing, each trace has 1024 samples at a 2-ms sample rate, and has a constant velocity of v = 10,000 ft/s. It has dipping events of 10, 20, 30, and 40 degrees, two scatterpoints, and two diffractions. The data were bandpass filtered with a maximum frequency of 50 Hz, allowing aliasing of dips greater than 26 degrees. This data were phase-shift migrated with a depth increment of 10 ft, to a maximum depth of 10,000ft, with the results shown on Figure 11b. Wrap-around energy is observed on the lower part of the section that could be controlled by methods such as zero-padding the traces, or attenuating the negative time data at each depth increment.

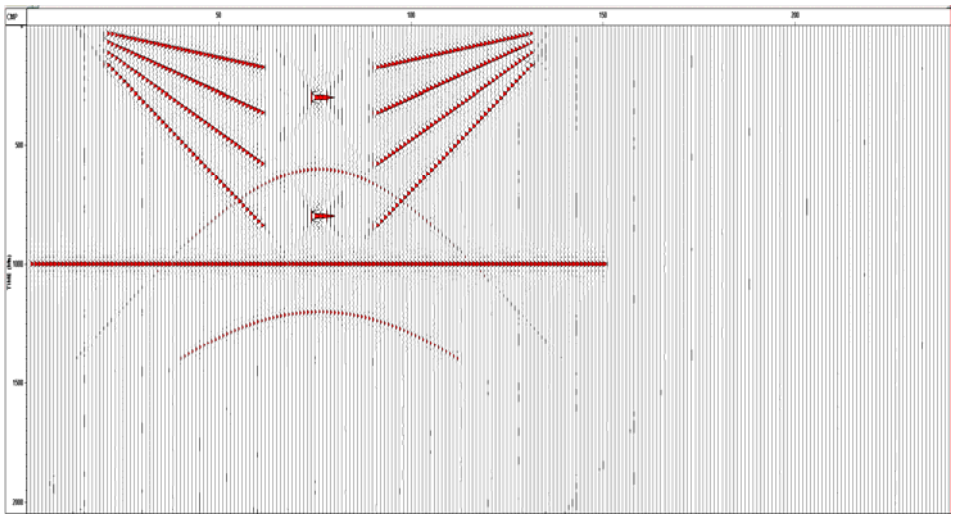

a)

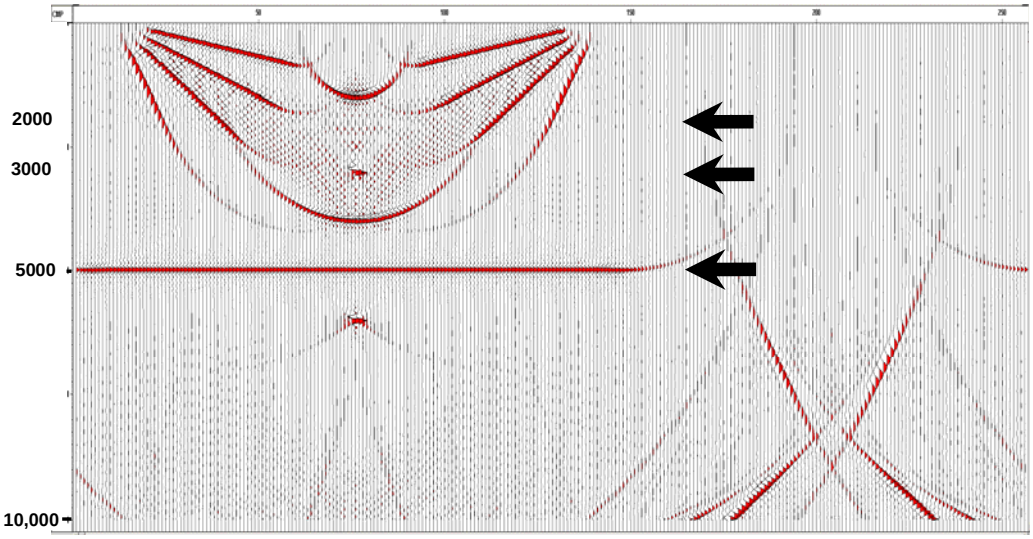

b

FIG. 11. Numerical data for phase-shift migration with a) the input and b) the migrated result.

Three time-sections at depth of 2,000 ft, 3,000 ft, and 5,000 ft downward are shown in Figure 12a–c, with the corresponding depths indicated on the migrated depth section. These section were computed in (k_x, ω) space then inverse Fourier transformed back into (x, t) space. It is the time-zero data in each of these sections that is copied to the migrated section. Note that, when the time section is at a depth of 5,000 ft, the horizontal reflector has move to $t = 0$, and is copied to the depth migrated section.

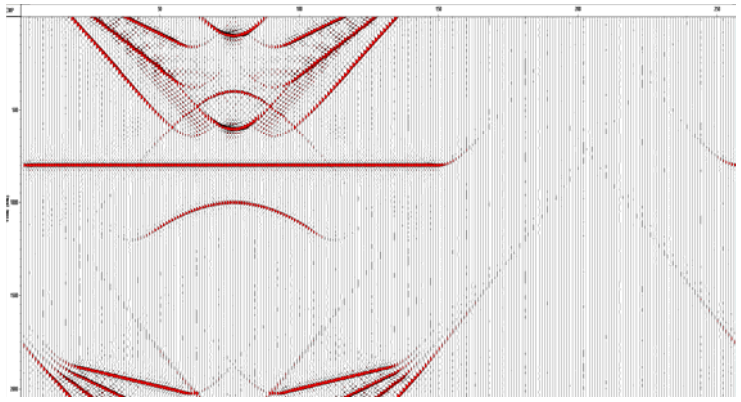

a)

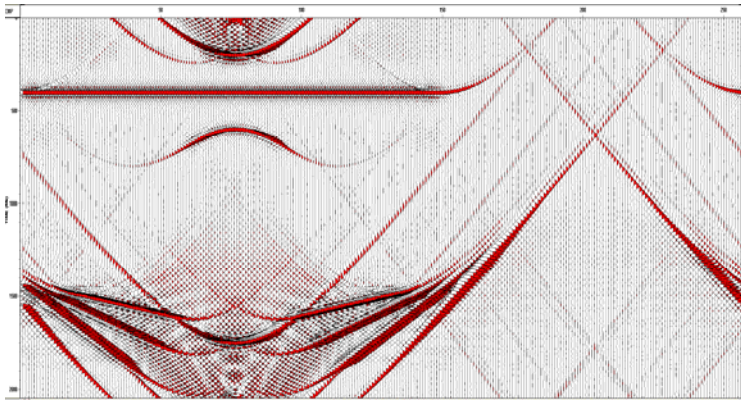

b)

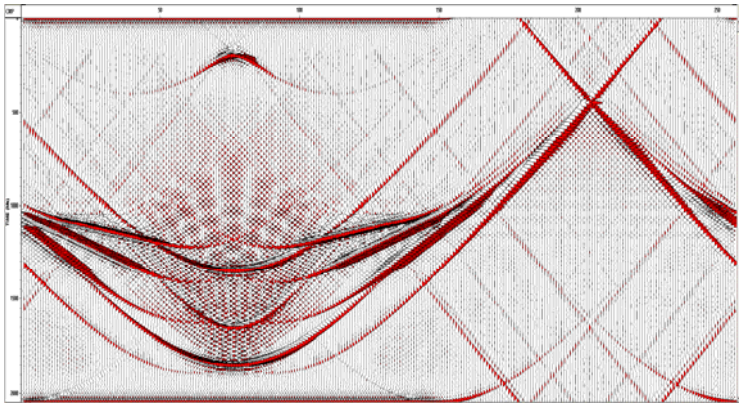

c)

FIG. 12. Downward-extrapolated time sections at depth of a) 2000 ft, b) 3000 ft, and c) 5000 ft, corresponding to the three arrows on the migrated section.

THE PHASE-SHIFT OPERATOR IN (K_X, ω), (X, ω), AND (X, T) SPACE

Phase-shift operator in (k_x, ω)

The phase-shift operator, $exp\left(-j\Delta z\sqrt{\frac{\omega^2}{v^2} - k_x^2}\right)$ may be visualized by the quiver plot in Figure 13, where points in (k_x,) space are plotted with arrows, where the length of the arrow represents the amplitude, and its angle defined by the phase. The wavenumber and frequency have been normalized for the quiver plot. The area of seismic energy is a complex exponential with a constant amplitude of unity and varying phase. The evanescent area, where the dips are greater than 45 degrees, contains real numbers (zero phase-shift) with amplitudes less than unity.

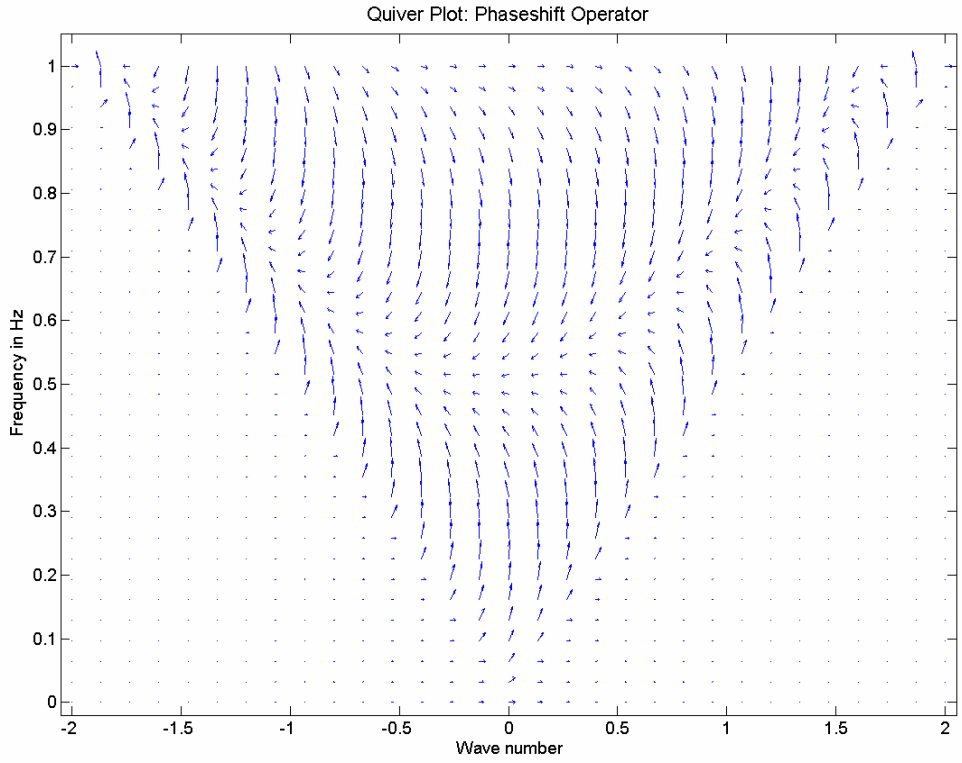

FIG. 13. Quiver diagram of phase-shift operator. (`PhaseShiftMigrationOpp.m`)

The amplitude and phase of the operator may also be plotted with colour representing amplitude and phase as indicated in Figure 14a. Data in these figures used typical parameters with a velocity of 3000 m/s, maximum frequency of 100 Hz, trace interval of 10 m, and a depth increment of 10 m. However, a dramatic image of the data is obtained by plotting the amplitude and phase as a 3-D surface in perspective view as shown in Figure 14c and d. Note the obvious areas of the operator where it is has unit amplitude and variable phase-shift, and the area with zero-phase and amplitudes less than unity.

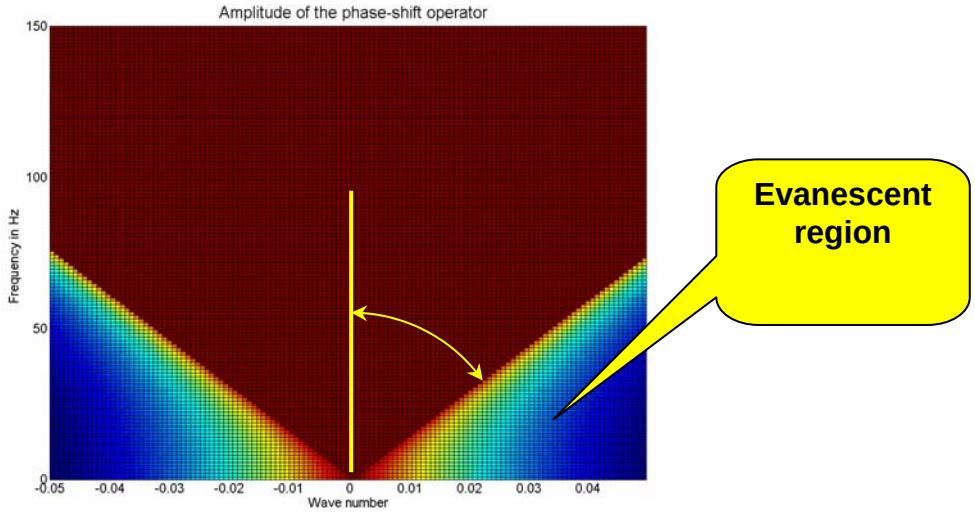

a)

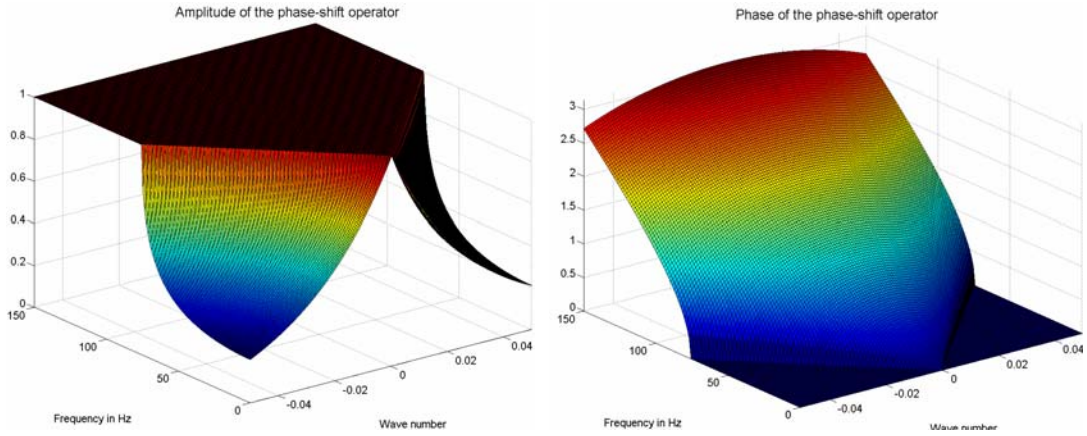

a) b)

FIG. 14. Phase-shift operator in (k_x, ω) space with a) the amplitude and b) the phase. (N_x = N_f = 128, d_x = 10 m, f_{max} = 150, V = 3000, del_z = 5 m)

These views provide significant insight into the phase-shift operator and were first brought to our attention this year by Kun Liu. Details of the operator at the boundaries become visually obvious, providing insight to methods for ensuring continuity, and aid in selecting parameters, as illustrated in Figure 15, that identify areas of concern for a typical phase-shift migration. The borders of this figure represent the Nyquist boundaries, where the amplitudes should have tended to zero as indicated. Simple corrections are identified in the following figure that provide band-limiting with a raised cosine bandwidth filter in the frequency direction, and a smaller trace interval of 3 m in the spatial direction. We point out at this time that the size of the trace interval is not determined by the phase-shift operator but by the data being migrated, causing potential problems.

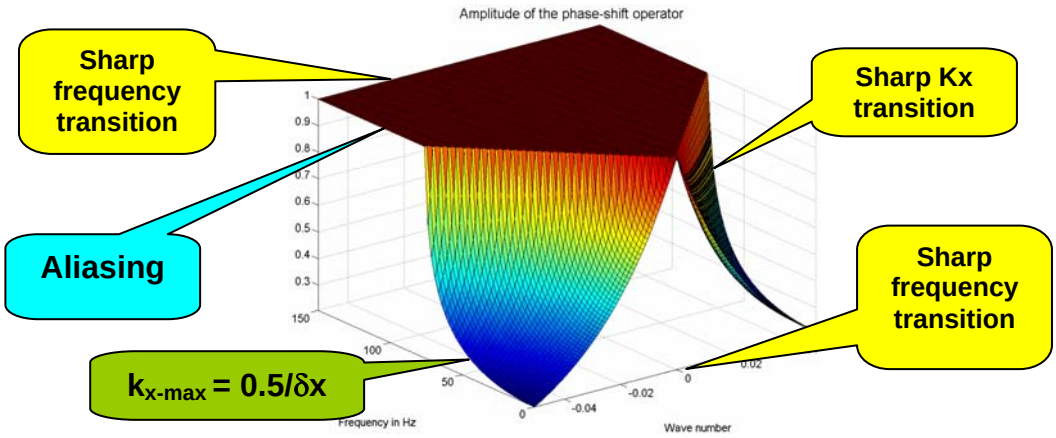

FIG. 15. The amplitude of the phase-shift operator with problems identified at the Nyquist boundaries.

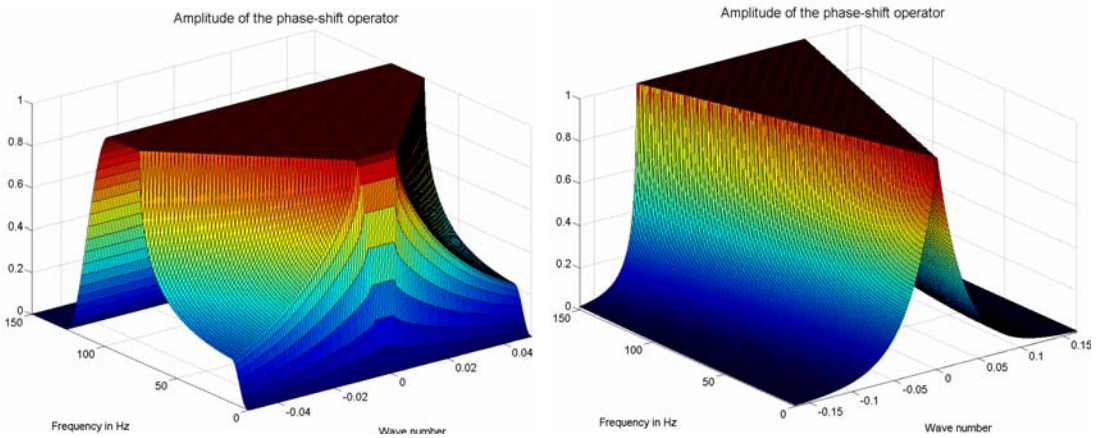

FIG. 16. Amplitude plots illustrating a) band-limiting the frequencies, and b) reducing the size of the trace interval.

The phase-shift operator in (k_x, ω), (x, ω), and (x, t) space

The simplicity of the perspective views of the phase-shift operator in (k_x, ω) space has lead naturally to similar views in (x, ω) and (x, t) space as shown in Figure 17.

Data in (x, ω) space were created by 1-D inverse-Fourier transforming the (k_x, ω) data at each frequency ω. The data still remains complex, with real and imaginary components shown in (c), and (d), with the magnitude shown in (e). Viewing the data in (x, ω) space is very useful in aiding the design of ωX operators. These operators are truncated in the spatial direction to a reasonable size for efficient migrations. The shaping and design of these operators is of continual interest and the main reason for this paper.

The inverse 1-D transform continues, but the data must now be conditioned to convert the complex frequency data into real time data. This is accomplished by creating a conjugate symmetry image of the (x, ω) space, and then inverse Fourier transforming each spatial array x. Views in this space show a "mini" Kirchhoff operator that can also be used to downward continue data. The 2-D size of this operator may also provide an indication of the spatial extent and its effect on dip limiting on the ωX operators.

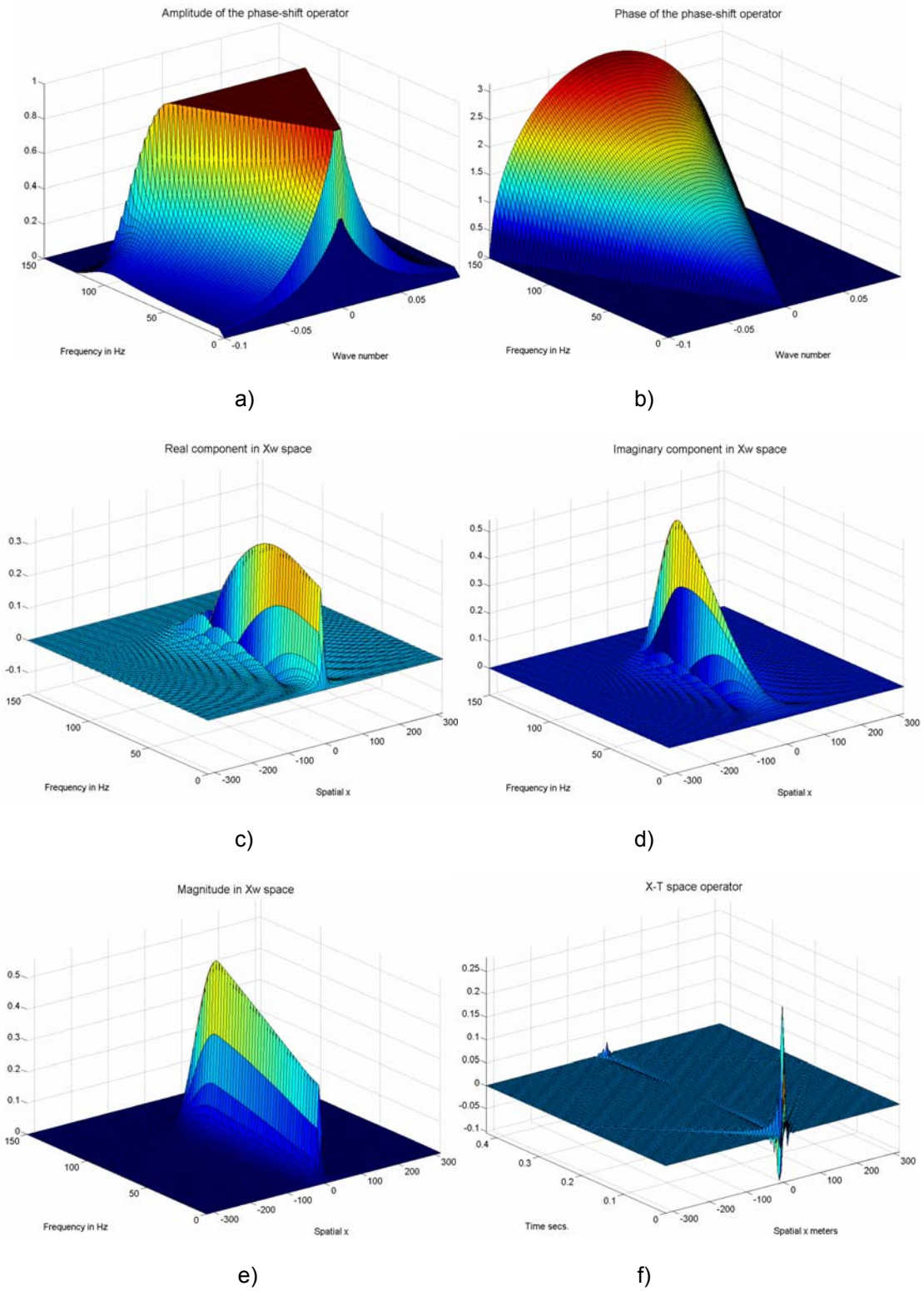

FIG. 17. The phase-shift operator showing a) the (k_x, ω) amplitude, b) the (k_x, ω) phase, c) the (x, ω) real, d) the (x, ω) imaginary, e) the (x, ω) magnitude and f) the (x, t) operator.

The phase-shift operator is capable of extrapolating surface data to any depth, and can provide an excellent image of an "ideal" Kirchhoff migration operator. Figure 18 shows

various perspective views of the (*x, t*) operator with an extrapolation depth of 250 m. Note the characteristic amplitude and shape of the operator. The frequencies of the operator were band-limited to some extent and display a wavelet shape. Image (d) is a side-view of the operator and hints at a typical phase rotation of the 45-degree, or Rho, filter for 2-D data. This operator could be used by using a 2-D convolution for each migrated point, but would be very inefficient, even if the convolution area was limited to a band around the central amplitude. In contrast, a traditional Kirchhoff migration only performs a line integral along the central peak of the (*x, t*) operator (ignoring aliasing).

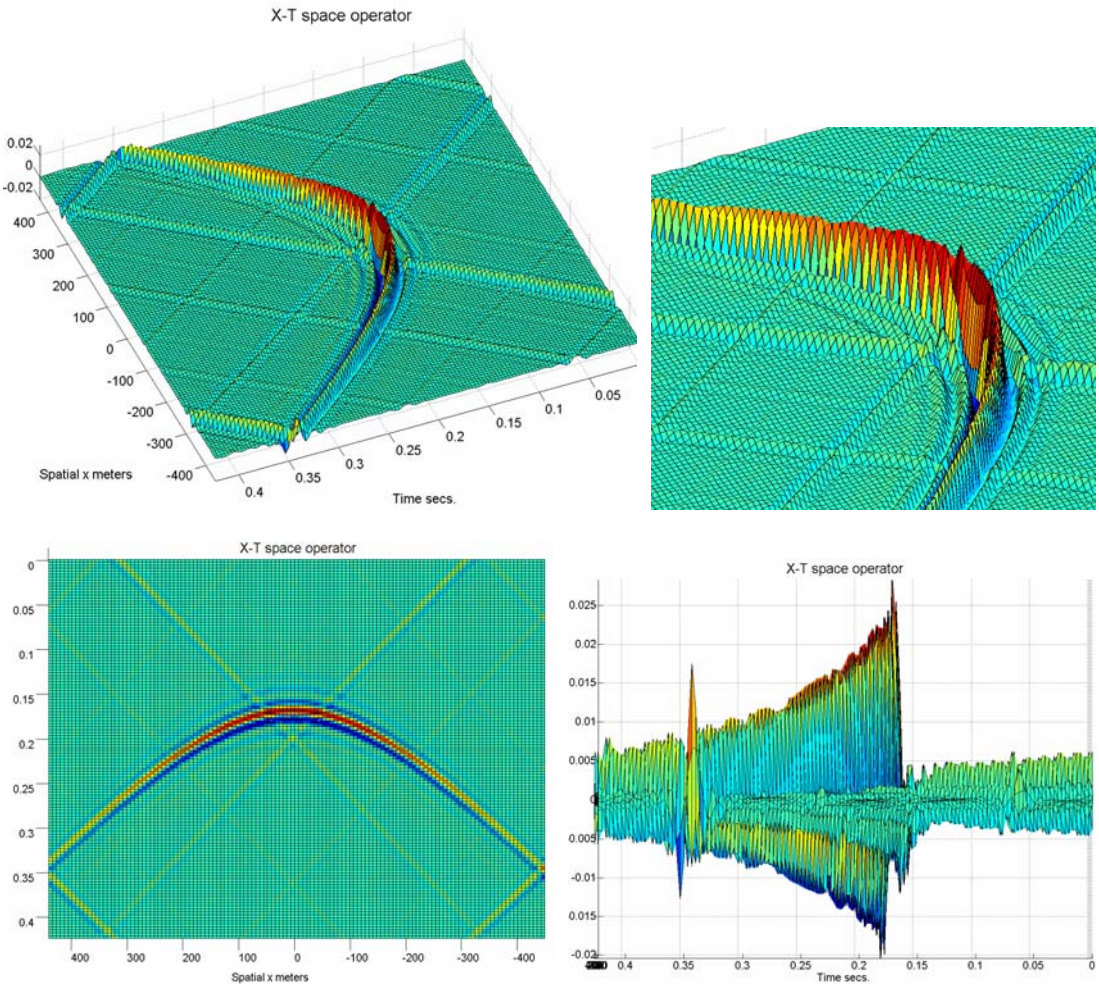

FIG. 18. The phase-shift operator in (*x, t*) space showing various perspective views.

The previous view of the phase-shift operator in (*x, t*) space for a small depth increment was difficult to visualize. Consequently the parameters were modified to produce a high resolution image, requiring a maximum frequency of 1000 Hz, and a spatial increment of 1 m, for a depth increment of 10 m. The results appear in Figure 19.

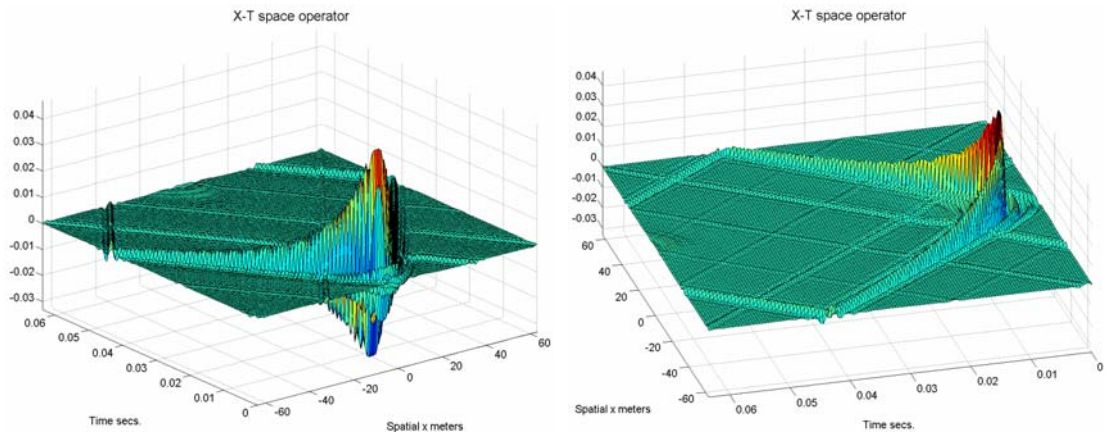

FIG. 19. Two perspective views of a high-resolution phase-shift operator in (x, t) space for a small depth increment of 10 m.

BUILDING AN *X* OPERATOR

An X operator for a given velocity and depth increment can be defined from a constant frequency slice of the (k_x, ω) operator as illustrated in Figure 20. This constant velocity operator is inverse transformed to (x, ω) space and truncated to a reasonable spatial width. The process of truncating an operator is equivalent to multiplying by a boxcar shaped filter. In the corresponding Fourier domain, that is equivalent to convolving with a sinc (sin$x$/x) function. Consequently, windowing the ωX operator in x space is equivalent to convolving the operator in the Kx domain with a sinc function as illustrated in series of images in Figure 21.

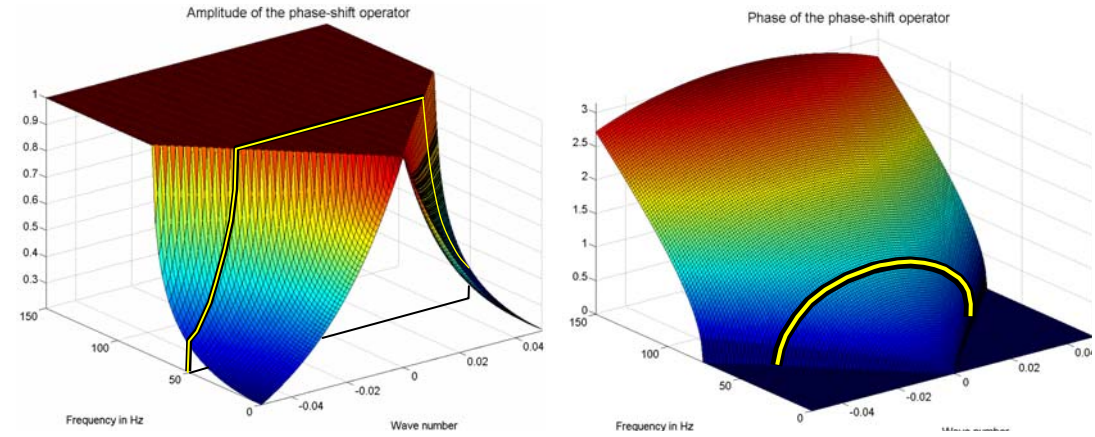

a) b)

FIG. 20. The phase-shift operator a) magnitude and b) phase in (x,) space showing the X operator at a constant frequency.

The construction of a boxcar-windowed ωX operator is illustrated in Figure 21. The magnitude and phase of the phase-shift operator in shown in parts (a) and (b) respectively. The corresponding magnitude, real, and imaginary components of the spatial operator are shown in (c) to (e) respectively. The actual shape is difficult to discern due to the large maximum distance required to minimize spatial aliasing. The

boxcar window and its Fourier transform are shown with relative size in (f) and (g). The truncated shape of the X operator is then displayed in (h) to (j). This operator is inverse transformed to K_x space and shown as the operators in (k) and (l).

The sharp corners of the original phase-shift operator in (k_x, ω) are now displaying a Gibb's phenomena distortion. This filter by itself is not a real problem, but we must consider that it, or a similar operator, will be applied many times, i.e. at each point for every downward extrapolation.

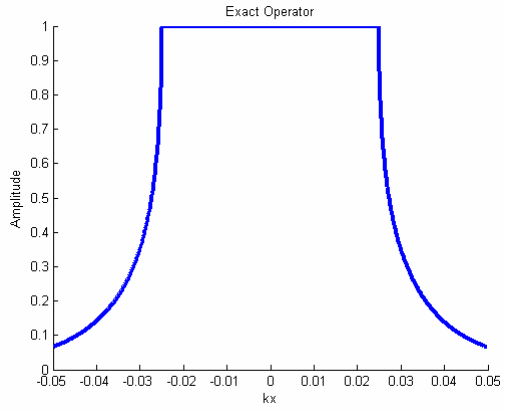

a) Magnitude of phase-shift operator **Kx**

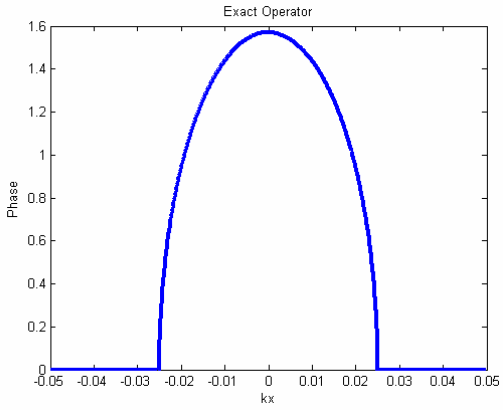

b) Phase of phase-shift operator in **Kx**

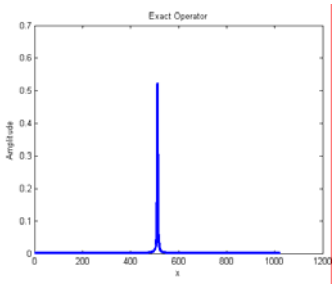

c) Magnitude in **x**

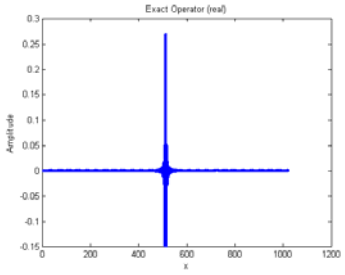

d) Real in **x**

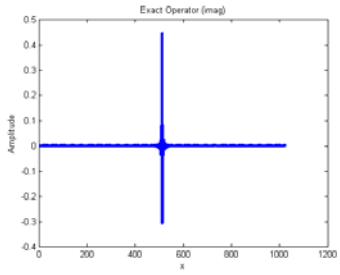

e) Imaginary in **x**

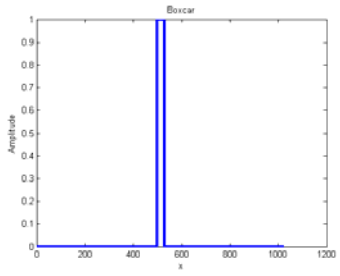

f) Window in **x**

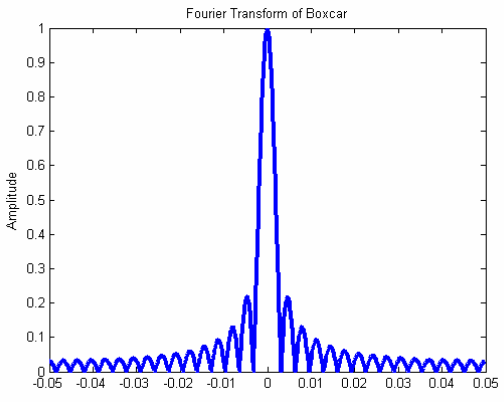

g) Window amplitude in **Kx**

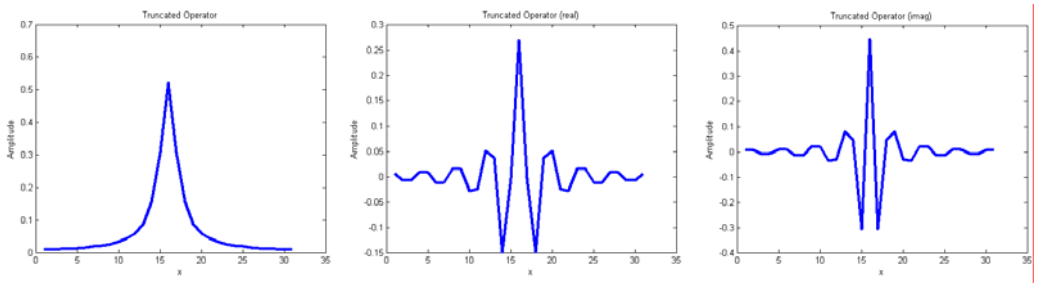

h) Magnitude i) Real windowed operator in **x** j) Imaginary

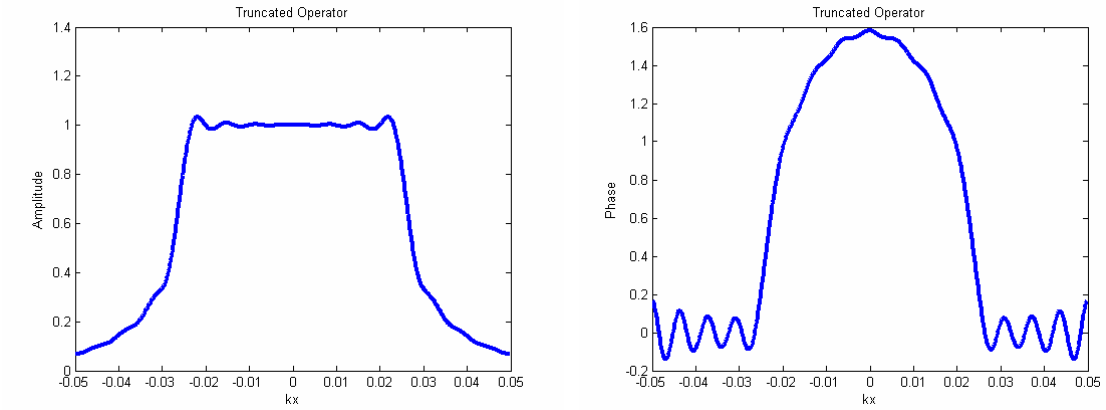

k) Magnitude l) Real

FIG. 21. Constant-frequency phase-shift operator progressing from a) k_x amplitude, b) k_x phase, c) x magnitude, d) x real, e) x imaginary, f) x boxcar window, g) k_x a sinc of the boxcar, h) the x magnitude of the windowed operator, i) x real operator, j) x imaginary operator, k) k_x magnitude, and l) the k_x phase.

The amplitude in the data area should be unity, but the Gibb's effect causes the amplitude to exceed unity to a possible value close to 1.05. As the convolutional operator is applied many times (say 500 to 5,000) in (x, ω) space, the effect is equivalent to multiplying the k_x operator by itself, or raising it to a power equal to the number of downward extrapolations. The very slight value of maximum ripple of 1.05 then becomes 1.05^N where N can be very large. For example, if $N = 100$, then $1.05^{100} = 131.5$. This very large amplitude is the source of instability. In addition, the values of amplitudes less than unity will become very small, producing severe distortion to the amplitude when the operator is applied many times. The source of this distortion was identified and illustrated to us by Kun Liu earlier this year. More recently, this distortion has been identified in a paper by Thorbecke (2004)

The above discussion used a boxcar or square shaped window to define the spatial operator. The boxcar may be the worst choice because of size of the Gibb's oscillations, but does identify the source of the oscillations, and it must always be remembered that any aperture-limited operator is always multiplied by this shape. Another and more traditional window to use is a Hanning window that is a raised cosine.

The above procedure of building an ωX operator was repeated, but a Hanning window was used instead of the boxcar. A much smoother K_x amplitude is obtained. The original

ωX operator, the boxcar designed operator, and Hanning windowed operator are shown in Figure 22. These three operators are each raised to a power of 10 in (d) to (f) and then to 100 in (g) to (i) to illustrate the effect on the operator for only 10 and 100 downward extrapolations. Note that the amplitude of the "Hanning 100" operator has significant attenuation of the higher wavenumbers, causing a dip-limiting effect on the migrated data.

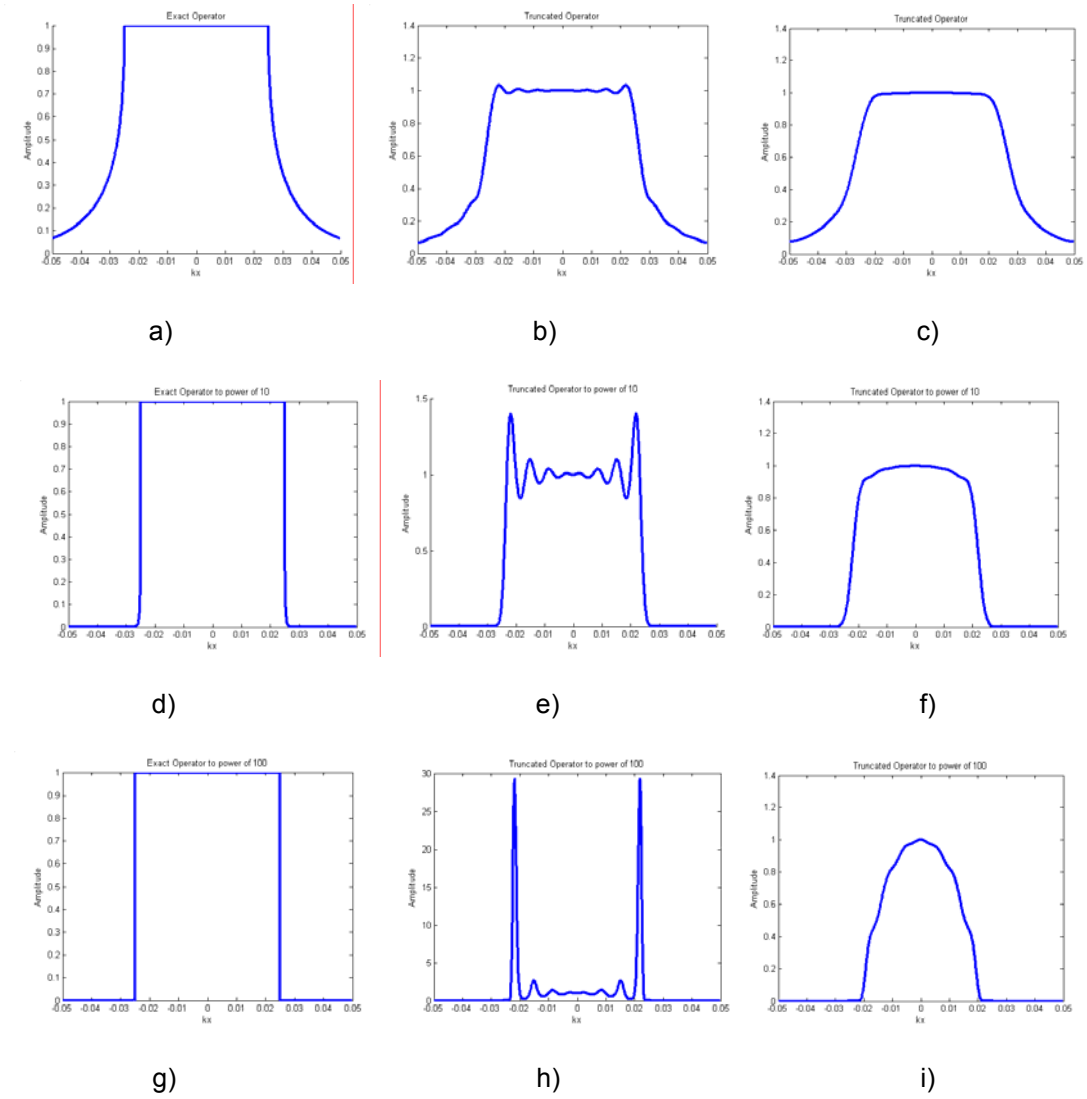

FIG. 22. Comparisons of the k_x operator amplitude for three window shapes and three powers of 1, 10 and 100: a) original phase-shift with power 1, b) boxcar window with power 1, c) Hanning window with power 1, d) original phase-shift with power 3, e) boxcar window with power 3, f) Hanning window with power 3, g) original phase-shift with power 10, h) boxcar window with power 10, i) Hanning window with power 10, `(PhaseShiftBoxHanningAll.m)`

A simple smooth operator, that illustrates the spatial size versus the attenuation of the ripple amplitude, may be designed by convolving a boxcar with itself many times. This process creates an operator or window shape that tends to a Gaussian distribution as illustrated in Figure 23, in which a three-point boxcar filter is convolved with the previous result 10 times. The shape progresses from a boxcar to a triangle, then a

quadratic, and then, very soon, to a Gaussian shape. The total size of the window is given by $2N+1$, where N is the number of convolutions — i.e., the size is 3, 5, 7, … .

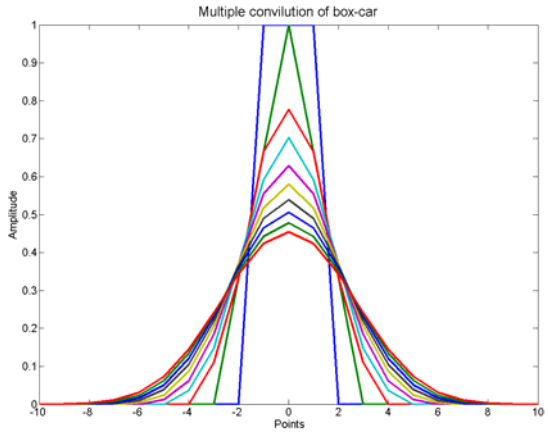

FIG. 23. Convolution of a three-point boxcar filter convolved with itself ten times.

A true Gaussian shape will Fourier transform to a true Gaussian shape. Therefore the transform of the convolved window will also tend to a Gaussian shape. However, the shape of the Fourier-transformed window is simply the sinc function raised to the power of N. This is illustrated in Figure 24, in which the boxcar window after 3 convolutions and after 10 convolutions is shown in (a). A corresponding sinc function, raised to the powers of 1, 3, and 10 are shown in (b). Even after 3 convolutions (or power of 3) both functions appear to be Gaussian.

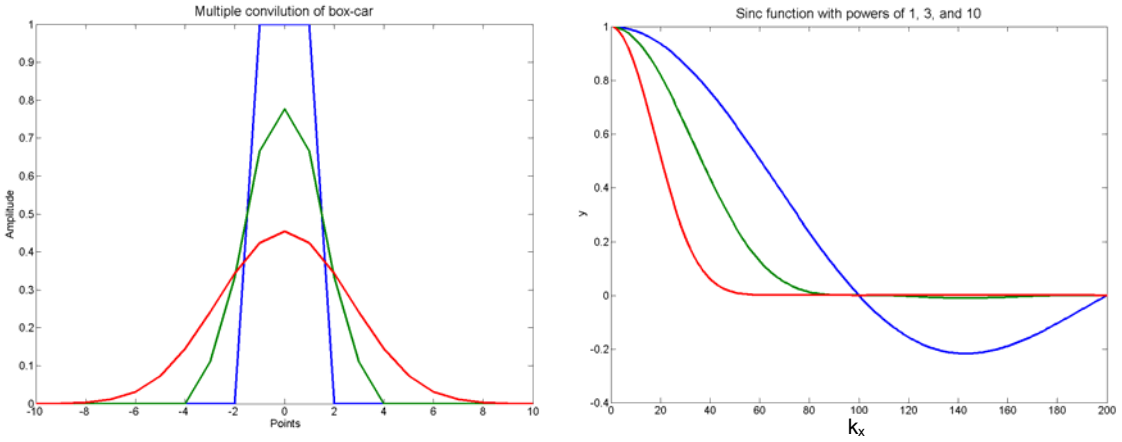

FIG. 24. Boxcar convolved 1, 3, and 10 times in a) x space; and b) the corresponding transforms in k_x space. `(GausianConvolution.m, sinxox.m)`

We are now in a position to relate the size of the window — produced by N multiple convolutions that produce a window width of $2N + 1$ — to the amplitude of the ripple that results from raising the sinc function to a power of N, (i.e. sinc^N). Gibb's phenomenon occurs when a discontinuity is convolved with a sinc or similar function. We will assume that the amplitude of the overshoot is directly related to the amplitude

of a portion on the sinc function before convolution. After N convolutions, this amplitude R will be

$$R = \delta^N . \tag{9}$$

Assume that the number of downward extrapolations is E, and that we desire the peak ripple after all extrapolations to be 1.5, i.e.,

$$\left(1+\delta^N\right)^E = 1.5 . \tag{10}$$

Since R is small, we take the first two terms of the series expansion to get

$$1 + E\delta^N = 1.5 . \tag{11}$$

Solving for N we get

$$N = \frac{\ln\left(\frac{0.5}{E}\right)}{\ln(\delta)}, \tag{12}$$

telling us that we can satisfy the ripple criteria with N convolutions that start with the boxcar shape.

For example, assume the number of iterations E = 500, and δ = 0.1, then N = 3. If the final number of points in a window is, for example, 31, then starting with a boxcar of 11 points, one convolution will give a triangular shape of 21 points, and a second convolution with the boxcar will produce a quadratic shape of 31 points.

COMMENTS

The dips on a section are limited with depth. The dip-limiting effects of the windowed operator also increases with depth. Consequently the combined effect may not be too serious.

When N is even, the amplitude of the sinc^N ringing will always be positive, and the amplitudes of the *kx* operator ring will be greater than unity, preventing ringing that may tend to zero.

CONCLUSIONS

The fundamentals of migration were presented with an emphasis on the phase-shift method. The phase-shift method in (k_x, ω) space was then extended to (x, ω) space, and then to (x, t) space. Plots of these surfaces were displayed to provide a visual foundation for the design of efficient (x, ω) space operators that allow the velocity to vary in both x and z. Illustrations of windowing the operator are included to illustrate the instabilities that arise due to "Gibb's phenomena".

An example of a smooth window, formed by convolving a boxcar with itself a number of times, was provided to illustrate how the window size is related to the amplitude ripple in the k_x transform of an (x, ω) operator.

In summary, when building an ωX operator, care must be taken to ensure a minimum ripple occurs to in the real data area of (k_x, ω) space. The amplitude must meet a criterion that is stable for the number of downward increments.

REFERENCES

Bancroft, J. C., 2004, A practical understanding of pre- and post-stack migration, Course Notes.

Thorbecke, J. W., Wapenaar, K., and Swinne, G., 2004, Design of one-way wavefield extrapolation operators, using smooth functions in WLSQ optimization, Geophysics: **69**, 1037–1045.

OBSERVATIONS

Note that the following red-tipped shark was observed cruising through the transforms during the preparation of this material. Caution should be taken when immersed in data.